Three-dimensional velocity map imaging: Setup and resolution improvement compared to three-dimensional ion imaging

S. Kauczok,[1] N. Gödecke,[1] A. I. Chichinin,[1,2] M. Veckenstedt,[1] C. Maul,[1] and K.-H. Gericke[1]
[1]*Institut für Physikalische und Theoretische Chemie, TU Braunschweig, 38106 Braunschweig, Germany*
[2]*Institute of Chemical Kinetics and Combustion, 630090 Novosibirsk, Russia*

(Received 14 April 2009; accepted 4 July 2009; published online 3 August 2009)

For many years the three-dimensional (3D) ion imaging technique has not benefited from the introduction of ion optics into the field of imaging in molecular dynamics. Thus, a lower resolution of kinetic energy as in comparable techniques making use of inhomogeneous electric fields was inevitable. This was basically due to the fact that a homogeneous electric field was needed in order to obtain the velocity component in the direction of the time of flight spectrometer axis. In our approach we superimpose an Einzel lens field with the homogeneous field. We use a simulation based technique to account for the distortion of the ion cloud caused by the inhomogeneous field. In order to demonstrate the gain in kinetic energy resolution compared to conventional 3D Ion Imaging, we use the spatial distribution of H^+ ions emerging from the photodissociation of HCl following the two photon excitation to the $V\ ^1\Sigma^+$ state. So far a figure of merit of approximately four has been achieved, which means in absolute numbers $\Delta v/v=0.022$ compared to 0.086 at $v \approx 17\,000$ m/s. However, this is not a theoretical limit of the technique, but due to our rather short TOF spectrometer (15 cm). The photodissociation of HBr near 243 nm has been used to recognize and eliminate systematic deviations between the simulation and the experimentally observed distribution. The technique has also proven to be essential for the precise measurement of translationally cold distributions. © *2009 American Institute of Physics.* [DOI: 10.1063/1.3186734]

I. INTRODUCTION

The spatial distribution of the reaction products in a reactive scattering experiment is vital to the understanding of the underlying dynamics of the reaction under scrutiny. Its measurement has always been one of the major goals ever since the pioneering work with crossed molecular beams by Lee and Herschbach.[1–5] First the one-dimensional projection of the three-dimensional (3D) distribution was measured by Doppler spectroscopy[6–8] and time of flight (TOF) spectrometry in photofragment translational spectroscopy.[9,10] Later the two-dimensional (2D) distribution became available by ion imaging[11] and velocity map imaging,[12] but it was still desirable to measure the full 3D distribution, as the 2D ion images need to be reconstructed under the assumption of cylindrical symmetry. Monitoring the full 3D information can be accomplished by either slicing through the 3D distribution with a time gated detector as realized in the slice imaging technique,[13] or by measuring all three components of the initial linear momentum of every single ion arriving at the detector with an inherently fast detector as the one developed by Dinu *et al.*[14] making use of the characteristic decay features of a phosphor screen together with a fast charge coupled device (CCD) camera or the commercially available combination of a microchannel plate (MCP) stack and a delay line anode (DLA) as in 3D ion imaging.[15] The latter technique has been used for several years now and has successfully been applied to a number of systems.[16–25] In the past couple of years it has become more and more widespread in the molecular dynamics community,[26,27] but a drawback of this technique has been so far the lower energy resolution compared to velocity map imaging, slice imaging, or the technique suggested by Vrakking, since these techniques make use of ion optics. The ion optics serve to compensate for the length of the excitation volume which smears out the velocity distribution in the direction of the laser beam, if a homogeneous field is applied und parallel ion trajectories are not focused onto one point. In this case the actually measured distribution is a convolution of the velocity distribution and the spatial ion source distribution. Until now, a homogeneous field has always been used in DLA based 3D ion imaging, since then the correlation between the data and the velocity components is fairly simple, i.e., the velocity component in the TOF spectrometer axis depends linearly upon the TOF if the field-free drift region is twice as long as the acceleration region (spatial focusing). Another point is the deterioration in time resolution caused by an inhomogeneous field, but this turns out to be overcompensated by the gain in spatial resolution and, since only the overall resolution yields well resolved speed distributions, is thus unimportant.

However, it should be emphasized that the true advantages of measuring the full 3D distribution over measuring a 2D projection—this includes the phosphor screen based 3D technique as an equally suited alternative—is the fact, that cylindrical symmetry needs not to be preserved, the data need not to be reconstructed by an Abel Inversion or a similar algorithm and coincidence measurements are possible. The slice imaging technique is in principle also capable of

measuring the full 3D distribution, but is not suitable for coincidence measurements and has the disadvantage, that most of the signal is not used. This is of course no problem if one has enough signal, but Coulomb repulsion of the individual ions gives a limitation for the number of ions that can be generated in one laser shot.

In this work we will show that the electric field geometry is no principal limitation whatsoever and the 3D velocity vector can be extracted from the data if an inhomogeneous electrical field is used. We choose a superposition of a homogeneous field with an Einzel lens field rather than a velocity mapping field derived from a Wiley McLaren geometry.[12] Also it should be pointed out, that in general with sufficiently fast electronics the repetition rate can be up to 20 kHz with the MCP-DL system which is not possible with the CCD-phosphor screen detection.

The general approach that we use is to first simulate the TOF spectrometer (SIMION©) and extract the correlation functions for the dependence of the velocity components on the impact coordinates and the TOF from simulated trajectories by fitting simple polynomials to the simulated data. In a second step, these functions are used for the interpretation of measured data from a well studied system in order to calibrate the procedure. After this, a general approach for the precise evaluation of data from any system is established. The whole procedure is implemented in a MATLAB©-program which also starts the SIMION.EXE and takes only a few minutes for a typical data set of 20 000 ions on a standard desktop computer.

For the calibration the H^+ distribution of the photodissociation of HBr near 243 nm is very suitable, since the energetics are precisely known.[28] The same is true for the H^+ distribution of the photodissociation of HCl following the two photon excitation to the $V\ ^1\Sigma^+$-state, since it has been studied thoroughly by several groups.[29–43] Therefore, the energy distribution is quite well established. Moreover, the speed distribution is well suited to characterize the speed resolution. There are two major peaks, one of which arises from the dissociation of HCl into H^+ and Cl^-. Thus, this peak should reflect the apparatus function, since this process is monoenergetic and isotope specific for a fixed wavelength. Therefore it is an adequate measure for the energy resolution of the technique. Under these conditions the figure of merit in speed resolution compared to the previous 3D ion imaging setup was estimated to be 3.9 ± 1.6.

The 3D Imaging resolution improvement presented here is similar to the one introduced to conventional 2D ion imaging by the velocity mapping concept of Eppink and Parker. One cannot expect the overall 3D resolution to be as good as the space resolution achieved in refined versions of the 2D velocity map imaging or slice imaging technique, e.g., reported by Loock and co-workers.[44,45] However, the superb 2D resolution of those experiments goes along with the complete loss of information about the third dimension, which has consequently been termed a "pancaking" or "ion sphere crushing" technique. Similarly, slicing techniques which can provide a very large spatial resolution and can be utilized without extraordinary efforts have the principal deficiency that for increased time resolution the slice approaches a mere sheet. Since a resolution increase consequently leads to the complete disappearance of the signal, a tradeoff between desired resolution, sufficiently high signal level and acceptable noise level has always to be made. Moreover, while it is possible in principle to record a full 3D distribution by shifting the slice, such measurements have not yet been reported, and again, for high temporal resolution a large number of slices would be needed to record the full 3D distribution and the synthesizing procedure is a tedious one.

It should be noted that the 3D velocity map imaging concept presented here is more than simply combining a standard DL detector with the standard 2D velocity map Imaging setup, a strategy, while relying on another type of fast position sensitive detector, was previously followed by Dinu *et al.*[14] It must be remembered in this context that the standard 2D velocity map Imaging concept relies on crushing the ion sphere to an almost 2D object (the "pancake"). The temporal peak broadening becomes very small, the symmetry of TOF peak broadening is lost, and the relationship between the velocity component v_z along the spectrometer axis and the deviation of the TOF from the TOF of a particle with zero velocity becomes highly nonlinear. However, in order to extract useful and precise information from the measured data in the third dimension the original shape of the ion sphere should not be too strongly distorted. Since this condition is not fulfilled for standard 2D velocity map imaging conditions the overall 3D energy resolution recorded by Vrakking *et al.* is inferior to the one reported here, despite a similar technical performance of the detection system, e.g., the TOF peak for I^+ ions with a total speed of 4 km/s is only 80 ns broad, whereas with the electrode and potential array presented here it would be $\sim 2.7\ \mu$s broad. Delayed extraction[13] could be also a way out of this dilemma.

Whenever cylindrically symmetric reaction dynamics systems are investigated 2D velocity map imaging or slicing remain very powerful tools which have been optimized and thus still yield better energy resolution than presented here. However, as already mentioned there is still a potential for optimization and for all other more complex systems not being cylindrical symmetric, 3D imaging in the velocity mapping variant reported here is inevitable. Its overall resolution can even be substantially improved over the values reported in this article by using a longer TOF spectrometer than the one used here. Whether a DLA based detector or a phosphor screen/multiple exposure camera combination is used is only of minor importance and may depend on the properties of the studied system. Alternatively, the slicing approach is also a very promising technique: Once the possibility of synthesizing 3D images from repeated slice measurements is successfully demonstrated, slicing may yield qualitatively similar information as 3D velocity map imaging.

II. EXPERIMENTAL SETUP

The apparatus for 3D velocity map imaging consists of a vacuum chamber which houses a TOF mass spectrometer, the detector and a pulsed nozzle for the generation of a supersonic molecular beam. The latter is either mounted

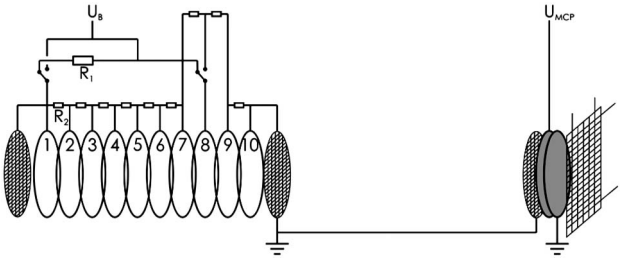

FIG. 1. Electrode and potential configuration of the TOF spectrometer. In the configuration shown, experiments are conducted with a skimmed molecular beam entering the spectrometer at a right angle with respect to the spectrometer axis.

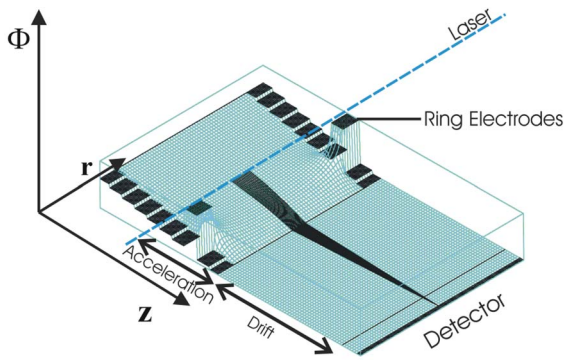

FIG. 2. (Color online) 2D representation of the cylindrically symmetric potential $\Phi(r,z)$ in the TOF spectrometer. The 15 ion trajectories shown have been computed with zero initial kinetic energy. The spectrometer is in the free beam setup.

directly to the first electrode of the TOF mass spectrometer (free beam setup for bimolecular reaction studies) or is situated in a separate chamber connected to the spectrometer chamber only by a skimmer in order to achieve differential pumping. The molecular beam is intersected at a right angle by two counter propagating laser beams for photodissociating precursors (ArF Optex 3, Coherent) and detection by resonance enhanced multiphoton ionization (REMPI) (Nd:yttrium aluminum garnet pumped Scanmate 2, Coherent). The parts vital to this contribution will be explained in more detail in the following subsections.

A. Vacuum system/molecular beam

To guarantee a sufficiently low background pressure (i.e., 10^{-7} mbar differentially pumped, 10^{-5} mbar free beam), the spectrometer chamber is pumped by two turbomolecular pumps (TMPs) (Pfeiffer TMU 260 P, 220 l/s each). If an experiment runs under differentially pumped conditions, the spectrometer chamber is connected to another vacuum chamber by a skimmer. The jet chamber is evacuated by one TMP (Pfeiffer TMU 521 P, 520 l/s). All TMPs are forepumped either by a combination of a small turbo molecular pump (Pfeiffer TMH 071 P) and a membrane pump (Pfeiffer MVP 015 T) or, in case the pumping system has to cope with higher quantities of gas, by a rotary vane pump filled with PFPE pump oil. The molecular beam is generated by a pulsed nozzle (General Valve, Series 9 Pulsed Valve), which is either mounted onto a rod on a *xyz*-moveable device in the jet-chamber (differentially pumped) or directly to the first electrode.

B. TOF spectrometer and detector

The TOF spectrometer was used in two different configurations, which do not differ from a principal point of view. A sketch of the setup used in the skimmed beam experiments is shown in Fig. 1.

It consists of an acceleration region which is attached to and separated by a grid from a field free drift region being twice as long as the acceleration region. This geometry for a one field spectrometer has first been reported by Wiley and McLaren[46] and has several advantages if the field gradient is constant. First, it automatically yields spatial focusing in the spectrometer axis *z*. Second, the relationship between the TOF and the *z*-velocity is linear and third it yields a good energy dispersion dt/dE suitable for 3D ion imaging. These characteristics are only slightly altered by the inhomogeneous field used here.

The acceleration region comprises ten ring electrodes with an inner diameter of 106 mm, which are kept apart by glass rods. They have an inner rim of 9 mm length and the distance between them is 1 mm. Thus, the acceleration region is close to being a tube with 1 mm spacing every 9 mm. This guarantees optimal shielding of external electrical fields and also makes the field very homogeneous near the electrodes.

In the skimmed beam configuration the antiparallel lasers and the molecular beam enter the stack of electrodes at a right angle between electrodes 5 and 6, making the effective acceleration region twice as long as the drift region. This configuration provides spatial focusing in the spectrometer axis as well as a linear relation between the TOF of individual ions and the velocity in this axis.

The supplied voltage (Stanford Research System, Model PS350) is either split by nine 2 MΩ resistors (R_2 in Fig. 1) in order to obtain a homogeneous electric field (ion imaging configuration), or applied to the eighth electrode which is connected to the first electrode by a 11 MΩ resistor (R_1) and the remainder split again uniformly (electrodes 7 and 9 are connected by two resistors, because the distance is two times longer). In this case the electrodes 7, 8, and 9 serve as an Einzel lens and their field is superimposed by a homogeneous field (velocity mapping configuration, Fig. 2). The actual voltage can precisely be measured by a Keithley 2000 multimeter. Voltages for the first electrode range between +100 and +1000 V generating an electric field from 10^4 to 10^3 V/m.

In the free beam configuration electrodes 1 to 4 are omitted and electrode 5 is replaced by a solid electrode henceforth referred to as repeller with a hole matching the front plate of the pulsed nozzle which is mounted directly onto it (Fig. 2). Thus, the only inhomogeneity to perturb the electric field near the repeller electrode is the 400 μm hole of the nozzle which is negligible.

In this case the repeller has ground potential and the last electrode and the drift region have a negative potential (typically between −500 and −50 V). For the lens electrode to

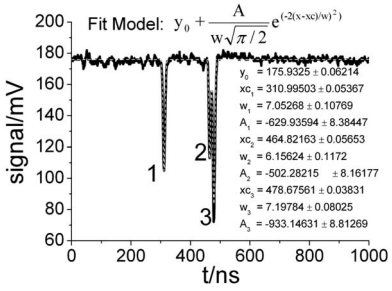

FIG. 3. Voltage as a function of time on one end of one DL after differential amplification as recorded by the oscilloscope. The three pulses belong to three different ions, each of them having respective counterparts on the other three DL ends. The parameters for a fit by three Gaussians including the standard deviations are shown. All four times for each ion together yield the point of impact (difference) and the TOF (sum).

have the highest potential this ought to be above ground potential and is taken from another Stanford PS350 voltage supply. Again, one can choose to run the spectrometer either in the homogeneous field mode or the Einzel lens mode by a simple switch.

After having passed the TOF spectrometer, the ions are projected onto a commercial 3D imaging detector (double stage multichannel plate (MCP) assembly+DL, Roentdek).[47,48] The eight signals from the four lines of the DL are decoupled from the high DL voltage, differentially amplified by an eight channel differential amplifier (KSU EDL DLA800), and finally recorded and analyzed by a LeCroy 500 MHz oscilloscope (Waverunner 6050, Quad 5 Gs/s). The individual ion signals are fit by Gaussians in order to determine the center of the electron cloud emerging from the MCP stack. From this the point of impact and the TOF for every ion detected are extracted.

C. Detector response characteristics

The replacement of the previously employed complex electronic system[15] for monitoring the DL outputs by a fast digital oscilloscope has three major advantages. First, from a technical point of view the read out system has become much simpler than before and as direct as possible. Second, monitoring DL pulse shapes and amplitudes becomes possible. This allows one to correlate matching pulses from both ends of the same DL, thus increasing the multihit capability of the detector. Third and most important, the detector resolution is significantly improved because fitting the DL pulses to a Gaussian function allows one to determine the center of the pulse with very high precision. This procedure is similar to the centroiding[49] strategy applied in 2D velocity map imaging where subpixel spatial resolution is realized by fitting a Gaussian function to the rather broad luminescent spot on the phosphor screen. Figure 3 shows a typical output of one end of one DL for a three particle hit event, after passing the differential preamplifier. These signals are directly fed into the oscilloscope for further data analysis. Similar outputs will be recorded for the opposite end of the same DL and for the two ends of the second DL oriented perpendicularly to the first one. The accuracy with which the center of the pulses can be determined depends on the pulse amplitude and lies typically between 50 and 100 ps. The impact position on the DL is determined from the time difference and the impact time from the time sum of matching pulses from both ends of the line. Both quantities can be determined with a precision better than 142 ps due to uncertainty propagation from the time measurements of the individual pulses. This means that the spatial resolution is between 35 and 71 μm. If a threshold for the pulse amplitude would be applied, this could be shifted toward the lower limit.

The measurement of the impact time determines the v_z component of the initial velocity vector of the particle which it has obtained in the investigated chemical process. Since total times of flight from initiating the process by the initiating laser until the impact of the particle on the detector are normally in the range of several microseconds, the relative temporal detector response uncertainty is of the order of 10^{-4} and can therefore completely be neglected compared to other experimental timing uncertainties, in particular the laser pulse duration of up to 5 ns. Because of this, the good temporal detector response is not used for the TOF resolution, but it is absolutely vital to the spatial resolution in the detector plane, which is not affected by an additive constant in the TOF, since it is canceled out of the equation. The method might also be employed with shorter laser pulses as well, e.g., femtosecond pulse lasers were used in the Dinu *et al.*[14] experiment. Then the total time resolution of the experiment is essentially given by the detector response time.

Of course, detector response characteristics set only a lower limit to the resolution power of an imaging experiment. Experimental uncertainties, such as spreads in starting time and position need to be taken into account and are normally more significant than the detector properties. Therefore, the kinetic energy resolution of an imaging setup should always be determined experimentally. For the experiments presented here, this is discussed in detail in Sec. V.

III. DETERMINATION OF LINEAR MOMENTUM

When the TOF spectrometer runs in the homogeneous field mode the velocity of an ion in the plane of the detector (v_r) is simply given by $v_r = r/t_{\mathrm{TOF}}$, where r refers to the length of the vector from the center of the ion cloud to the point of impact on the detector. The velocity component perpendicular to the detector plane (v_z) is directly proportional to the difference of the actual TOF t_{TOF} and the TOF of an ion with zero velocity in the z-axis (t_0), i.e., $v_z = P^*(t_{\mathrm{TOF}} - t_0)$. The parameter P can be calculated directly from the field parameters and refined by considering the symmetry of the measured ion cloud itself.

In case the machine runs in the Einzel lens mode, the determination of the velocity from the data is more intricate. In principle, the ion trajectories can be calculated from theory. For this we need to calculate the electric potential in the acceleration region of the mass spectrometer, cylindrical symmetry of the potential provided. We need to calculate the potential function $\Phi(r,z)$ in cylindrical coordinates ($0 \le r \le R$, $0 \le z \le L$, where L is the length of the acceleration region and R is its radius), which obeys the Laplace equation

$$\frac{1}{r}\frac{\partial}{\partial r}\left(r\frac{\partial \Phi}{\partial r}\right)+\frac{\partial^2 \Phi}{\partial r^2}=0. \quad (1)$$

The boundary conditions suitable for our spectrometer can be written as $\Phi(r,z=0)=0$, $\Phi(r=R,z)=f(z)$, and $\Phi(r,z=L)=-\Phi_a$. The boundary potential function in the case of a homogeneous electric field is $f_{\mathrm{hf}}(z)=-z\Phi_a/L$. In the case of the Einzel lens configuration it is $f_{\mathrm{lens}}(z)=-z\Phi_a/L+\Delta f_{\mathrm{lens}}(z)$, where $\Delta f_{\mathrm{lens}}(z)$ is the change of boundary potential due to the positive voltage on the third ring electrode. Hence the solution of Eq. (1) is $\Phi_{\mathrm{lens}}=\Phi_{\mathrm{hf}}+\Delta\Phi$, where $\Delta\Phi$ is a solution of Eq. (1) with the boundary conditions $\Phi(r,z=0)=\Phi(r,z=L)=0$, $\Phi(r=R,z)=\Delta f_{\mathrm{lens}}(z)$ and Φ_{hf} is the potential of the homogeneous field without the lens, i.e., $\Phi_{\mathrm{hf}}=-z\Phi_a/L$. The solution $\Delta\Phi$ is known from the literature.[50] Hence the final expression for the solution of Eq. (1) for our potential array is given by Eqs. (2) and (3),

$$\Phi(r,z)=\Phi_{\mathrm{hf}}(z)+\Delta\Phi(r,z)=-z\Phi_a/L+\sum_{n=1}^{\infty} f_n\frac{I_0(\pi nr/L)}{I_0(\pi na/L)}\sin(\pi nz/L), \quad (2)$$

$$f_n=(2/L)\int_0^L f(z)\sin(\pi nz/L)dz. \quad (3)$$

Here $I_0(x)$ denotes the zeroth order Bessel function. Thus, from this analytical potential the ion trajectories can be calculated.

However, the problem is inverted in a way that the initial velocities must be calculated from the point of impact and the TOF rather than calculating the trajectories from the field and the initial conditions. For this reason and because the potential difference between the last grid and the MCP of the order of 1.5 kV over a distance of 7 mm also has to be included, we choose a different approach based upon a simulation by the program SIMION©, instead of devising an algorithm which makes use of the analytical potential. The procedure of the experiment and its analysis can be divided into three parts.

(1) The potential for the lens electrode is adjusted so that ions with zero velocity starting from different points in the plane of the ion source are focused on one point within the accuracy given.
(2) The precise voltages are applied in the experiment and the deviation due to the finite stability of the system is measured to five digit precision.
(3) Trajectories are simulated for defined initial velocities in order to obtain the corresponding times of flight and coordinates on the detector (x,y) using the exact measured potentials. Appropriate functions are fitted to the simulated data which are then used to interpret any other data set.

It turns out that unlike in 3D ion imaging the x,y-coordinates only depend on the initial in-plane velocity v_r, regardless of the TOF or v_z. Of course this is only true within a certain range of kinetic energy where spherical aberrations are negligible (Fig. 4). At first glance this seems to be surprising, because in ordinary 3D ion imaging one has

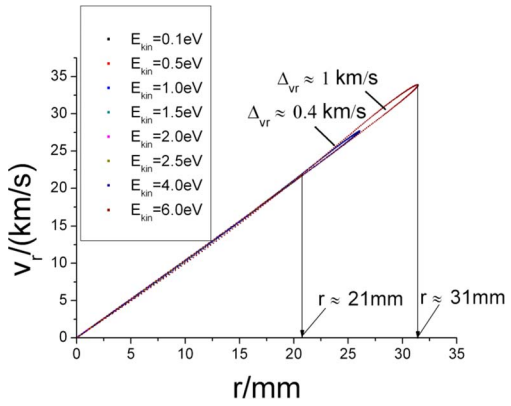

FIG. 4. (Color online) Simulated (SIMION©) dependence of the radial velocity component of H^+ ions on the total distance from the center of the MCP for different total kinetic energies. The azimuthal angle is varied over 180°. The acceleration voltage is −150 V and the lens voltage +165 V. The increasing importance of spherical aberrations becomes apparent when the detector area is more than half filled ($r>20$ mm).

the obvious relation $v_r=r/t$. However, the difference in TOF translates to a different starting point in the source plane for which to compensate the TOF spectrometer has been originally setup.

As can be seen from Figs. 4 and 5, v_r depends essentially linearly on r, but under further scrutiny a straight line through the origin does not describe the simulation sufficiently and therefore a small quadratic correction leads to a perceptible improvement (Fig. 5). Figure 4 also shows the onset of an increasing effect of spherical aberrations. These depend on the radius at which the ion trajectory passes the lens electrode, which is given by the ratio of the field energy and the initial kinetic energy at a given solid angle. Thus, for a given kinetic energy one cannot simply decrease the acceleration voltage to cover the whole area of the detector with the fragment distribution. The available area of the MCP is thus fixed by the total length of the spectrometer (leaving the lens electrode in its place). The longer the TOF spectrometer is, the larger is the acceleration voltage needed to cover the whole MCP with a fragment cloud with a given maximum kinetic energy. This has the effect that the radius at which the

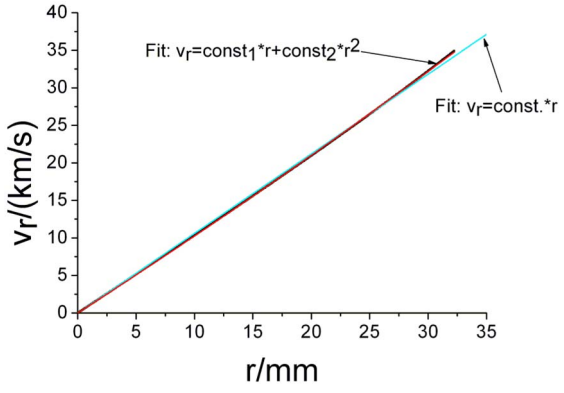

FIG. 5. (Color online) Simulated (SIMION©) dependence of the radial velocity component of H^+ ions on the total distance from the center of the MCP for a fixed azimuthal angle of 90°. The slight curvature which is best described by a quadratic correction can be seen in the comparison between the two fit curves (red and light blue) with the simulated data (black curve).

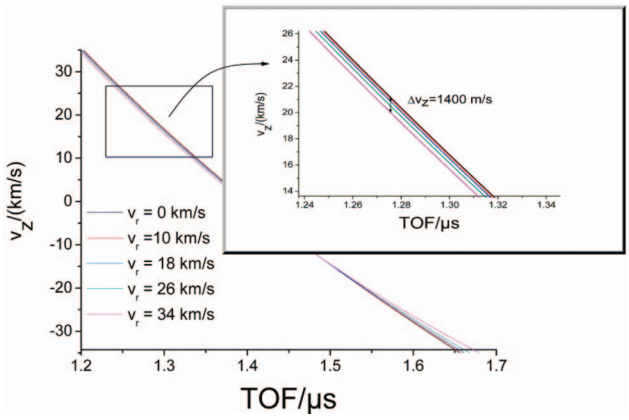

FIG. 6. (Color) Simulated dependence of v_z on the TOF for different v_r for H^+ at −150 V acceleration and +165 V lens potential as simulated by SIMION©. The necessity to include the respective v_r is highlighted in the magnification of the detail in the rectangular area.

ion trajectories pass the lens is smaller. Considering Eq. (4) which describes the force acting on the ion, this means that the higher order terms become negligible and only the linear part remains. In this case the conditions are optimal for focusing parallel trajectories, since the gain of inward momentum is linear with respect to the radius r if the time Δt to pass the lens is constant, i.e., the velocity in the propagation direction must be the same. Otherwise chromatic aberrations are to be expected. If the TOF spectrometer is longer, the kinetic energy due to acceleration is also larger, making the spread in Δt and thus chromatic aberrations due to the initial velocity distribution smaller. These two features are desired effects of the lens and the respective trajectories behave like paraxial and monochromatic light beams in normal optics,[50]

$$m\frac{\partial^2 r}{\partial t^2} = e\left(\frac{r}{2}\frac{\partial^2 \Phi}{\partial z^2} + \frac{r^3}{8}\frac{\partial^4 \Phi}{\partial z^4} + \frac{r^5}{384}\frac{\partial^6 \Phi}{\partial z 6} + \ldots\right). \tag{4}$$

For the determination of v_z (see Fig. 6) one needs to include the dependence on the in plane velocity v_r, since with increasing v_r the "bump" in the potential which needs to be overcome by the ion on its way to the detector increases (Fig. 2). The effect of the size of the v_r-component on v_z is not always a delay as one might first think, but actually depends on the value of v_z. For example, for all positive values of v_z, the ion with a higher v_r-component arrives slightly earlier at the detector than its counterpart with lower v_r.

From this it seems sensible to first determine v_r [Eq. (5)] and then v_z using the value of v_r [Eqs. (6) and (7)],

$$v_r(r) = \sum_i a_{r,i} r^i \quad (i = 1,2), \tag{5}$$

$$v_z(v_r,t) = \sum_i a_{z,i}(v_r) t^i \quad (i = 0,1,2), \tag{6}$$

$$a_{iz}(v_r) = \sum_j b_{i,j} v_r^j \quad (j = 0-6). \tag{7}$$

In principle one might think, more of the MCP's surface could be covered if the spherical aberrations could be simply included in the model. Then v_r would be considered a function of r and t. This would only be correct if the ion source would be a single point, which of course is not the case. Since t scales as $\cosh(r_0)$, with r_0 being the initial radial position from which the trajectory starts, this would in fact lower the kinetic energy resolution.

Due to the fact that the shape of the trajectories of the ions only depends on the kinetic energy and not on the mass, one only needs to run the simulations for one mass. To apply the results to a different mass than hydrogen, one only needs to take into account that the particle with mass m_p needs a factor of $(m_P/m_H)^{1/2}$ more time to run through the trajectory. This fact can be expressed by Eqs. (8)–(10),

$$t_H = \sqrt{\frac{m_H}{m_p}}, \tag{8}$$

$$v_{z,p} = v_{z,H}[t_H, v_{r,H}(r)]\sqrt{\frac{m_H}{m_p}}, \tag{9}$$

$$v_{r,p}(r) = \sqrt{\frac{m_H}{m_p}} v_{r,H}(r). \tag{10}$$

IV. EXPERIMENTAL CALIBRATION

In this chapter we show measurements of the H^+ distribution emerging from the photodissociation of HBr which were recorded in the free beam setup and therefore do not represent the inherent energy resolution of the technique. Using the equations derived from the SIMION© simulations, one should first test them on a well studied system. This is what we used the photodissociation of HBr around 241.135 nm for, since this is a convenient wavelength to detect H atoms by [2+1]-REMPI. Additionally, only one color is needed for the experiment. In this way problems that are connected with experiments employing two lasers, such as proper overlap in time and space do not have to be considered. The dye laser was scanned over the REMPI-transition in order to eliminate any bias in the detection resulting from the Doppler Effect.

The measured data displayed as a meridian plot and a speed distribution in Fig. 7 have been evaluated by the procedure described in Sec. III (a meridian plot is a projection of a point (v_x, v_y, v_z) into a plane containing the origin while the absolute speed $|v|$ is left constant[15]). In order to eliminate the visual effect of the anisotropy of the process, a projection into the x,z-plane with the electric field vector pointing in the y direction has been chosen.

To account for any discrepancy of the model and the reality, calibration factors for v_r and v_z have been fit to the two shells of measured H fragments belonging to the bromine leaving in the $^2P_{3/2}$ and the $^2P_{1/2}$ state, respectively, using the dissociation energy of 3.758 eV (Ref. 51) and the energy for the spin-orbit excitation of 0.457 eV (Ref. 52) (red lines in Figs. 7 and 8). It turns out that the factor to correct the radial velocity component is negligibly different from one, whereas the z component has to be multiplied by a factor of 0.97. The reason for this lies in the fact that the data shown in Fig. 7 have been recorded in the free beam setup with a total distance from the nozzle to the laser beam of ~5 mm. Thus the source of the ion trajectories is spread out over a range on the order of 1 cm in the plane. The effect of

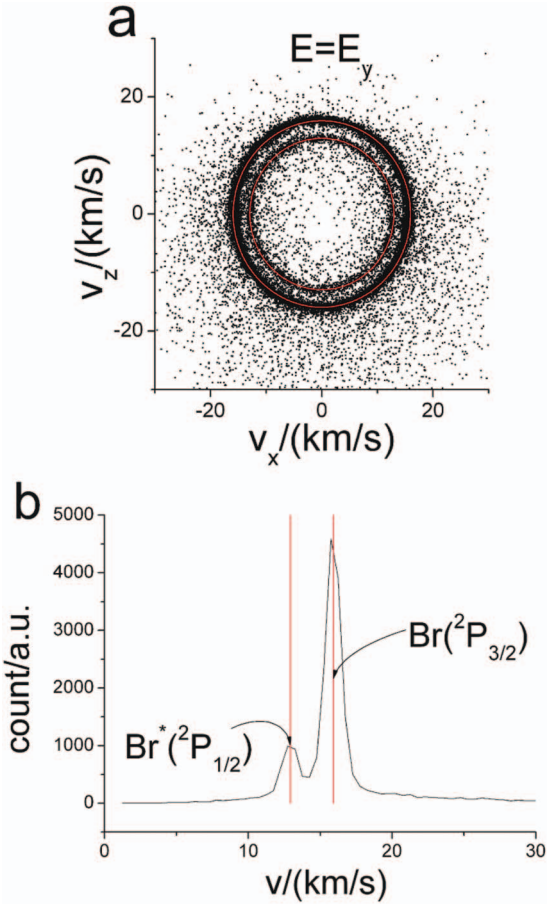

FIG. 7. (Color) (a) Corrected meridian plot (see text and Ref. 15) of H-atoms emerging from the photodissociation of HBr at 241.135 nm (black) and theoretical values calculated from the dissociation energy and the spin orbital splitting (red). The data do not represent the inherent energy resolution of the technique. (b) H^+ ion speed distribution of the measurement in (a). The red lines denote the theoretical values for the dissociation into $H+Br(^2P_{1/2})$ and $H+Br(^2P_{3/2})$, respectively. The data do not represent the inherent energy resolution of the technique.

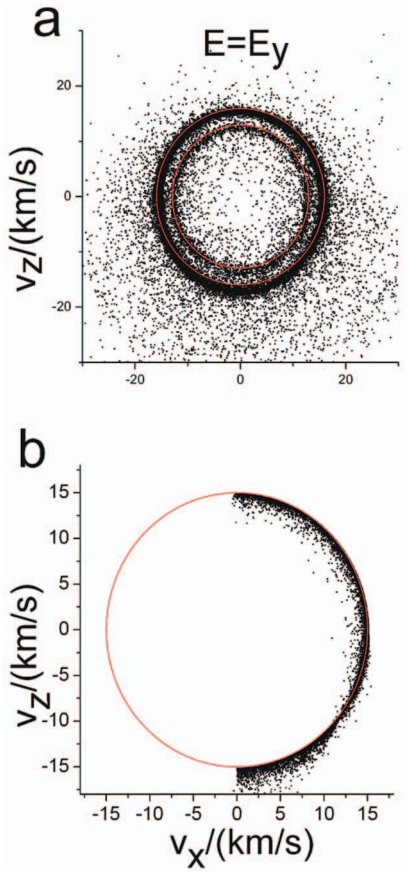

FIG. 8. (Color) (a) Experimental data of Fig. 6 shifted in the z direction in order to highlight the coincidence of the upper outer and lower inner rim of the ion cloud with the theoretical value (red). This shows that the apparent stretch of the z axis and the broadness of the speed distribution can be explained by the effect of the source distribution in the free beam setup. (b) Simulation: coincidence of the upper outer and lower inner rim of the ion cloud with the theoretical value (red) (Gaussian distribution of the ion source in the x,y plane).

this is that the further away from the center of the spectrometer an ion starts, the later it arrives at the detector compared to the identical ion starting from the center. Additionally this effect is asymmetric with respect to ions which initially fly toward the detector and those which initially fly away from the detector. Since this effect is not included in the simulation, the effect of it on the z vector components assigned by the analysis is a shift to lower z velocities and a spread in the velocity distribution in the z axis. This can be inferred from Fig. 8. There the coincidence of the theoretical value (red circle) with the highest values of the distribution on the z axis in the upper and the lower part of the distribution is shown for a simulation with a Gaussian source distribution with a full width at half maximum of 10 mm [Fig. 8(b)] and the measured values which have been shifted accordingly [Fig. 7(a)]. At least 70% - the scaling factor to match the red ring is 0.99—of the stretch of the z axis can be explained by this effect. The rest may be due to a feature of the real setup not taken into account in the simulation.

V. KINETIC ENERGY RESOLUTION

Since the HBr data have been measured using the free beam setup, they are not an appropriate example for the actual gain in kinetic energy resolution by the employment of the Einzel lens. In order to depict the advantage of the technique over conventional 3D ion imaging, Figs. 9 and 10 show a comparison of H^+ distributions emerging from the photodissociation of HCl in the $V\,^1\Sigma^+$ ($v=12$, $J=0$) state recorded with the standard 3D ion imaging technique and with 3D velocity map imaging, respectively. The data have been recorded with a skimmed molecular beam.

The detailed dynamics of this process have been investigated in detail by our group and by Loock and co-workers.[23,44,45] Only peak II in Fig. 9(b) is important for the determination of the resolution, since this peak emerges from the dissociation into H^+ and Cl^- which do not have any internal excitation (peak I and the propagation of peaks denoted as III are due to the dissociation of super excited HCl states yielding $H(n=2)$ atoms and the photodissociation of vibrationally excited HCl^+, respectively,[23,44,45]). Therefore the width of peak II reflects solely the apparatus function. The standard deviation σ of peak II is approximately 350 ms^{-1}. This number varies of course with the mass of the particle and the maximum kinetic energy in the process under scrutiny and has to be compared to the studied process. To determine the speed resolution of the standard technique

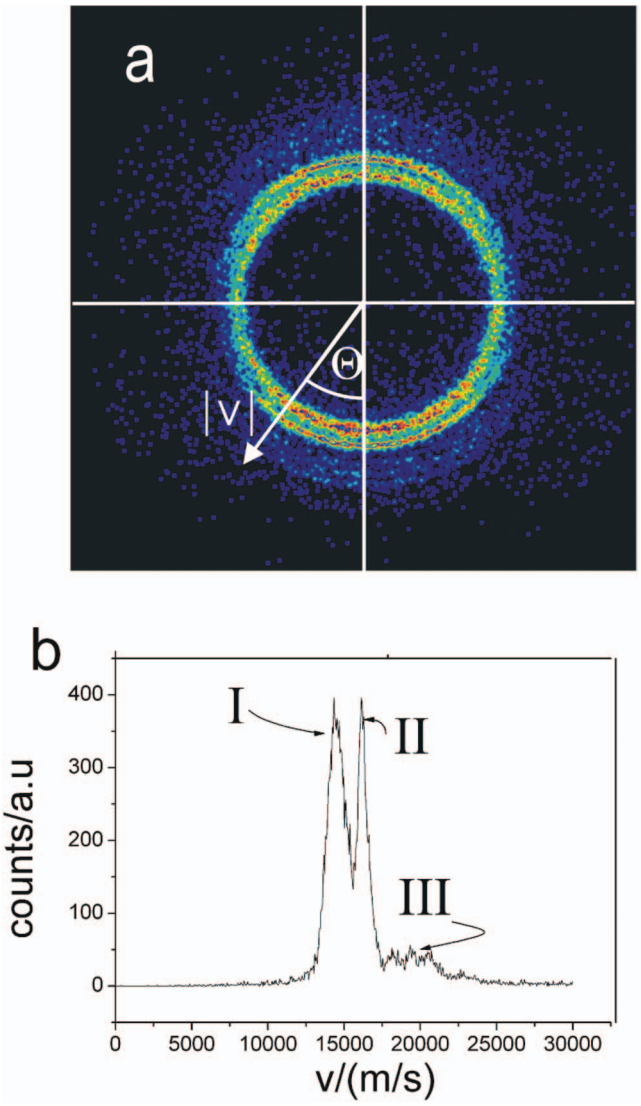

FIG. 9. (Color) (a) Density map of the meridian plot (see text and Ref. 15) of the H^+ ions emerging from the photodissociation of HCl starting from the $V\,^1\Sigma^+$ $(v=12,J=0)$ state recorded using the Einzel lens setup and a skimmed molecular beam. b: Speed distribution of the data shown in a. Only peak II is relevant for the determination of the kinetic energy resolution since it emerges from the dissociation into H^+ and Cl^-. For the explanation of the other peaks, see text and Refs. 23, 44, and 45.

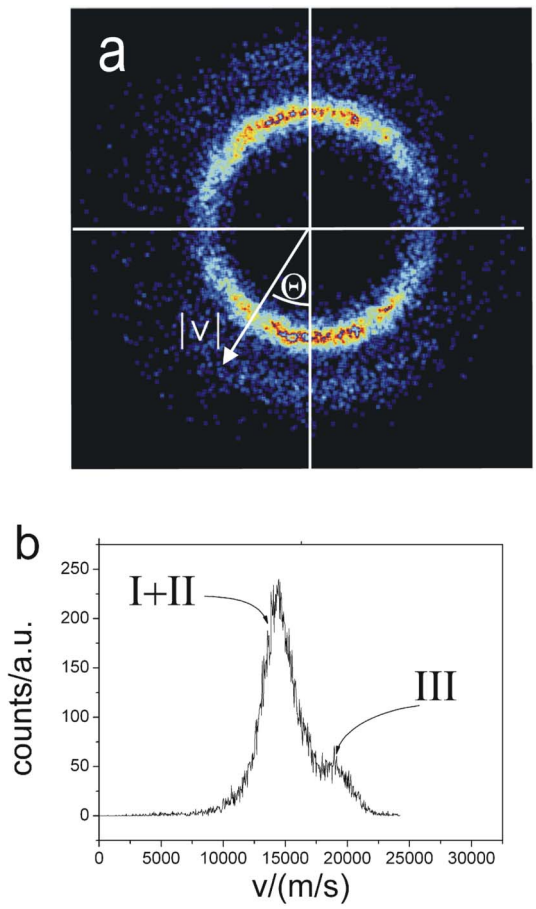

FIG. 10. (Color online) (a) Conventional 3D ion imaging data, density map of the meridian plot (see text and Ref. 15) of the same H^+ distribution as in Fig. 8, recorded using a homogeneous acceleration field and a skimmed molecular beam. (b) Speed distribution of the data in (a). Peak I and II are merged completely and no structure in the peak propagation III can be discerned. For the explanation of the underlying dynamics of the dissociation process, see text and Refs. 23, 44, and 45.

one can take the difference of the two major peaks in Fig. 10(a) (~ 1740 ms^{-1}) as a measure for the maximum resolution and the difference of the two peaks in Fig. 10(b) (~ 4105 ms^{-1}) as one for the minimum speed resolution, as they do not appear as two separated peaks, if they have the same height or area. Taking into account that the distance between two Gaussians to be discernible as separated should be at least 2σ, the standard deviation can be estimated to be 1461 ± 591 or $\Delta v/v = 0.086 \pm 0.035$ at $v \approx 17\,000$ m/s. The relative speed resolution of the 3D velocity mapping technique is therefore $\Delta v/v = 0.022$ at $v \approx 17\,000$ m/s, i.e., the figure of merit is 3.9 ± 1.6. However, it should be pointed out that this is not a theoretical limit to the technique, but reflects only the comparatively short TOF spectrometer and the presence of two meshes. Nevertheless the approach presented here is general and these technical limitations can be overcome, if a higher resolution is desired (see Sec. III).

Another circumstance, under which the switching to velocity map imaging proves to be very useful is the recording of very slow photofragments in the case of the molecular beam being oriented perpendicularly to the spectrometer axis. This is favorable for photodissociation processes, since the ions are immediately extracted from the high density region in the molecular beam and the molecular beam can be directed into a turbo molecular pump. In this case the maximum TOF is limited by the fact that the molecules should not hit the walls of the spectrometer. Thus, the distribution cannot be blown up to a size at which the length of the laser focus becomes negligible. Figure 11 shows the comparison of NO products from the intracluster reaction shown in Eq. (11) recorded with 3D velocity map imaging [Fig. 11(a)] and conventional 3D ion imaging [Fig. 11(b)].[2]

$$N_2O \cdot N_2O \xrightarrow{h\nu} N_2 + O(^1D) \cdot N_2O \rightarrow NO + NO + N_2. \quad (11)$$

A very distinct feature of this reaction is that the back scattered NO molecules (in the center of mass system of the collision) are very slow in the laboratory frame (with a translational temperature $T_{trans} \approx 150$ K), and thus it constitutes

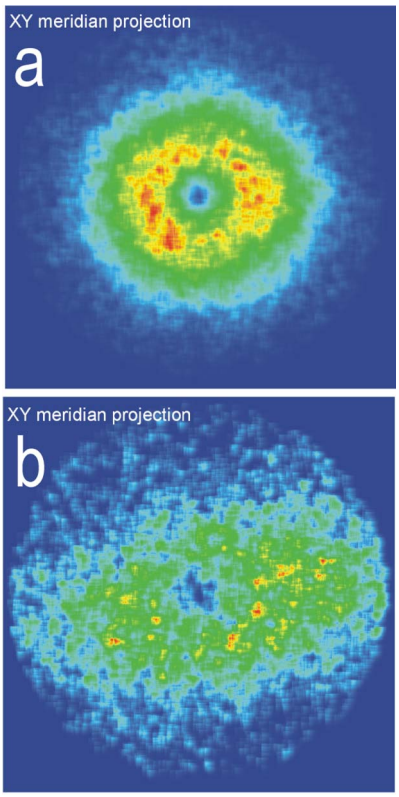

FIG. 11. (Color online) (a) Density map of a meridian plot (see text and Ref. 15) of NO products emerging from the reaction in Eq. (11) recorded with 3D velocity map imaging. (b) Density map of a meridian plot of NO products emerging from the reaction in Eq. (11) recorded with conventional 3D ion imaging.

one of these special cases (for a detailed analysis of the dynamics see Refs. 23 and 24).

As can be seen, an evaluation of the picture in Fig. 11(b), which has been recorded in the ion imaging mode, would have been hardly possible. The reason for the prolate shape of the distribution is the length of excitation volume.

VI. CONCLUSIONS AND OUTLOOK

In this contribution we report on our approach toward the employment of ion optics in 3D ion imaging. The advantages of 3D ion imaging—direct observation of all three components of the product velocity vector—and of the velocity map imaging technique—improved spatial resolution due to the elimination of the effect of the finite observation volume—are combined. In this present work a figure of merit of 3.9 ± 1.6 with respect to the improvement of speed resolution has been achieved under the given experimental conditions (H^+ distribution from the photodissociation of the $V\ ^1\Sigma^+$ state of HCl), corresponding to a 3D velocity resolution of $\Delta v/v$ 0.022. With regard to the established 2D solution first reported by Parker and Eppink,[12] we suggest the term 3D velocity map imaging for this technique. Although the electrical field we use is different, the actual velocity of the ions is mapped instead of a convolution of the velocity with the ion source distribution.

We have solved the problem of velocity assignment to the raw data, i.e., point of impact on the detector and TOF for each ion, by using a forward simulation by the program SIMION©. From this we infer the correlation functions needed to analyze the data [Eqs. (5)–(7)]. The approach is general and can be applied to all kinds of field geometries.

In order to calibrate the system experimentally, the H^+ distribution resulting from the photodissociation of HBr near 243.135 nm has been used. A significant deviation has only been found for the component in the TOF spectrometer axis of the product velocity vector which has been explained to be mostly due to the effect of the finite observation volume on the TOF. The deviation is on the order of a few percent (typically 2%–3%) for different field parameters and a procedure for quantitative correction has been presented.

The onset of spherical aberrations for larger speeds determines the area of the MCP's surface that can be covered by ions for a given geometry, i.e., the total length of the TOF spectrometer. For additional improvement beyond the one presented here it would be therefore desirable to have a vacuum system which allows a much longer TOF spectrometer.

ACKNOWLEDGMENTS

Financial support by the Deutsche Forschungsgemeinschaft and the Alexander von Humboldt foundation is gratefully acknowledged.

[1] Y. T. Lee, J. D. Mc Donald, P. R. Le Breton, and D. R. Herschbach, Rev. Sci. Instrum. **40**, 1402 (1969).
[2] Y. T. Lee, Angew. Chem. **99**, 967 (1987).
[3] Y. T. Lee, Angew. Chem. Int. Ed. Engl. **26**, 939 (1987).
[4] D. R. Herschbach, Angew. Chem. **99**, 1251 (1987).
[5] D. R. Herschbach, Angew. Chem. Int. Ed. Engl. **26**, 1221 (1987).
[6] E. J. Murphy, J. H. Brophy, G. S. Arnold, W. L. Dimpfl, and J. L. Kinsey, J. Chem. Phys. **70**, 5910 (1979).
[7] B. Katz, J. Park, S. Satyapal, S. Tasaki, A. Chattopadhyay, W. Yi, and R. Bersohn, Faraday Discuss. Chem. Soc. **91**, 73 (1991).
[8] D.-C. Che and K. Liu, J. Chem. Phys. **103**, 5164 (1995).
[9] R. W. Diesen, J. C. Wahr, and S. E. Adler, J. Chem. Phys. **50**, 3635 (1969).
[10] S. J. Riley and K. R. Wilson, Faraday Discuss. Chem. Soc. **53**, 132 (1972).
[11] D. W. Chandler and P. L. Houston, J. Chem. Phys. **87**, 1445 (1987).
[12] A. T. J. B. Eppink and D. H. Parker, Rev. Sci. Instrum. **68**, 3477 (1997).
[13] C. R. Gebhardt, T. P. Rakitzis, P. C. Samartzis, V. Ladopoulos, and T. N. Kitsopoulos, Rev. Sci. Instrum. **72**, 3848 (2001).
[14] L. Dinu, A. T. J. B. Eppink, F. Rosca-Pruna, H. L. Offerhaus, W. J. van der Zande, and M. J. J. Vrakking, Rev. Sci. Instrum. **73**, 4206 (2002).
[15] A. Chichinin, T. Einfeld, C. Maul, and K.-H. Gericke, Rev. Sci. Instrum. **73**, 1856 (2002).
[16] T. Einfeld, A. I. Chichinin, C. Maul, and K.-H. Gericke, J. Chem. Phys. **116**, 2803 (2002).
[17] T. Einfeld, A. I. Chichinin, C. Maul, and K.-H. Gericke, J. Chem. Phys. **117**, 1123 (2002).
[18] T. Einfeld, A. I. Chichinin, C. Maul, and K.-H. Gericke, J. Chem. Phys. **117**, 4214 (2002).
[19] A. I. Chichinin, T. Einfeld, C. Maul, and K.-H. Gericke, Chem. Phys. Lett. **390**, 50 (2004).
[20] L. Schäfer, N. Gödecke, O. Ott, C. Maul, K.-H. Gericke, P. S. Shternin, E. V. Orlenko, and O. S. Vasyutinskii, Chem. Phys. **301**, 213 (2004).
[21] A. I. Chichinin, T. Einfeld, K.-H. Gericke, J. Grunenberg, C. Maul, and L. Schäfer, Phys. Chem. Chem. Phys. **7**, 301 (2005).
[22] A. I. Chichinin, T. Einfeld, C. Maul, and K.-H. Gericke, Dokl. Phys. Chem. **402**, 96 (2005).
[23] A. I. Chichinin, C. Maul, and K.-H. Gericke, J. Chem. Phys. **124**, 224324 (2006).
[24] A. I. Chichinin, P. S. Shternin, N. Gödecke, S. Kauczok, C. Maul, O. S. Vasyutinskii, and K.-H. Gericke, J. Chem. Phys. **125**, 034310 (2006).
[25] C. Maul, S. Kauczok, N. Gödecke, K.-H. Gericke, and R. Delmdahl, Physik Journal **6**, 88 (2007).

[26] N. T. Goldberg, K. Koszinowski, A. E. Pomerantz, and R. N. Zare, J. Chem. Phys. **125**, 133503 (2006).
[27] O. Geßner, E. T.-H. Chrysostom, A. M. D. Lee, D. M. Wardlaw, M.-L. Ho, S.-J. Lee, B.-M. Cheng, M. Z. Zgierski, I.-C. Chen, J. P. Shaffer, C. C. Hayden, and A. Stolow, Faraday Discuss. **127**, 193 (2004).
[28] M. W. Chase, Jr., J. Phys. Chem. Ref. Data Monogr. **9**, 429 (1998).
[29] S. Arepalli, N. Presser, D. Robie, and R. J. Gordon, Chem. Phys. Lett. **118**, 88 (1985).
[30] R. Callaghan, S. Arepalli, and R. J. Gordon, J. Chem. Phys. **86**, 5273 (1987).
[31] T. A. Spiglanin, D. W. Chandler, and D. H. Parker, Chem. Phys. Lett. **137**, 414 (1987).
[32] E. de Beer, B. G. Koenders, M. P. Koopmans, and C. A. de Lange, J. Chem. Soc., Faraday Trans. **86**, 2035 (1990).
[33] D. S. Green, G. A. Bickel, and S. C. Wallace, J. Mol. Spectrosc. **150**, 354 (1991).
[34] D. S. Green, G. A. Bickel, and S. C. Wallace, J. Mol. Spectrosc. **150**, 388 (1991).
[35] D. S. Green, G. A. Bickel, and S. C. Wallace, J. Mol. Spectrosc. **150**, 303 (1991).
[36] Y. Xie, P. T. A. Reilly, S. Chilukuri, and R. J. Gordon, J. Chem. Phys. **95**, 854 (1991).
[37] D. S. Green and S. C. Wallace, J. Chem. Phys. **96**, 5857 (1992).
[38] A. Kvaran, A. Logadottir, and H. Wang, J. Chem. Phys. **109**, 5856 (1998).
[39] K. Wang and V. McKoy, J. Chem. Phys. **95**, 8718 (1991).
[40] E. de Beer, W. J. Buma, and C. A. de Lange, J. Chem. Phys. **99**, 3252 (1993).
[41] A. Holzwarth, M. Penno, and K.-M. Weitzel, Mol. Phys. **97**, 43 (1999).
[42] M. Michel, M. V. Korolkov, M. Malow, K. Brembs, and K.-M. Weitzel, Phys. Chem. Chem. Phys. **3**, 2253 (2001).
[43] A. Kvaran and H. Wang, Mol. Phys. **100**, 3513 (2002).
[44] C. Romanescu, S. Manzhos, D. Boldovsky, J. Clarke, and H.-P. Loock, J. Chem. Phys. **120**, 767 (2004).
[45] C. Romanescu and H.-P. Loock, J. Chem. Phys. **127**, 124304 (2007).
[46] W. C. Wiley and I. H. McLaren, Rev. Sci. Instrum. **26**, 1150 (1955).
[47] I. Ali, R. Dörner, O. Jagutzki, S. Nüttgens, V. Mergel, L. Spielberger, K. Khayyat, T. Vogt, and H. Bräuning, Nucl. Instrum. Methods Phys. Res. B **149**, 490 (1999).
[48] O. Jagutzki, V. Mergel, K. Ullmann-Pfleger, L. Spielberger, U. Spillmann, R. Dorner, and H. Schmidt-Bocking, Nucl. Instrum. Methods Phys. Res. A **477**, 244 (2002).
[49] B.-Y. Chang, R. C. Hoetzlein, J. A. Mueller, J. D. Geiser, and P. L. Houston, Rev. Sci. Instrum. **69**, 1665 (1998).
[50] J. Picht, Ann. Phys. **407**, 926 (1932).
[51] K. P. Huber and G. Herzberg, *Molecular Spectra and Molecular Structure: IV. Constants of Diatomic Molecules* (Van Nostrand Reinold, New York, 1950), Vol. 4.
[52] C. E. Moore, *Atomic Energy Levels*, Natl. Bur. Stand. (U.S.) Circ. NoU.S. GPO, Washington, DC, 1971), Vol. 1; C. E. Moore, *Atomic Energy Levels*, Natl. Bur. Stand. (U.S.) Circ. NoU.S. GPO, Washington, DC, 1971), Vol. 2.